

Electronic structure of 30° twisted double bilayer grapheneGuodong Yu^{1,2}, Zewen Wu¹, Zhen Zhan¹, Mikhail I. Katsnelson², and Shengjun Yuan^{1,2,*}¹Key Laboratory of Artificial Micro- and Nano-Structures of Ministry of Education and School of Physics and Technology, Wuhan University, Wuhan 430072, China²Institute for Molecules and Materials, Radboud University, Heijendaalseweg 135, NL-6525 AJ Nijmegen, The Netherlands

(Received 12 May 2020; accepted 31 August 2020; published 10 September 2020)

The electronic structures of 30° twisted double bilayer graphene, which loses the translational symmetry due to the incommensurate twist angle, are studied by means of the tight-binding approximation. We demonstrate the interlayer decoupling across the 30° twisted interface in the vicinity of the Fermi level from various electronic properties, including the density of states, effective band structure, optical conductivity, and Landau-level spectrum. However, at Q points, the interlayer coupling results in the appearance of new Van Hove singularities in the density of states, new peaks in the optical conductivity and, importantly, the 12-fold-symmetry-like electronic states. The k -space tight-binding method is adopted to explain this phenomenon. The electronic states at Q points show charge distribution patterns more complex than the 30° twisted bilayer graphene due to the symmetry decrease. These phenomena also appear in the graphene monolayer on the AB-stacked graphene bilayer with a 30° twist angle.

DOI: [10.1103/PhysRevB.102.115123](https://doi.org/10.1103/PhysRevB.102.115123)**I. INTRODUCTION**

In theory, twisted bilayer graphene (TBG) can transform from a crystalline (commensurate configuration) to a quasicrystalline (incommensurate configuration), depending on the twist angle [1]. At a large twist angle ($\theta > 15^\circ$), the TBG has electronic properties similar to those of two decoupled graphene monolayers [2–9]. The Fermi velocity is renormalized by decreasing the twist angle [10,11]. At the so-called magic angle ($\theta \sim 1.1^\circ$), the Fermi velocity becomes zero and the moiré flat bands appear in the vicinity of the Fermi level [10,12]. Accordingly, the TBG at the small twist angle as a model system of strongly correlated electrons has drawn much attention due to novel electronic properties, such as the unconventional superconductivity [13–15] and correlated insulator phases [16].

The 30° TBG, an incommensurate bilayer configuration, has been grown successfully on H-SiC(0001) [17], Pt(111) [18], Cu-Ni(111) [19], and Cu [20,21] surfaces. As the first two-dimensional quasicrystal based on graphene, 30° TBG has received increasing attention both experimentally and theoretically [22–28]. A method to grow high-quality 30° TBG epitaxially on SiC using borazine as a surfactant has also been proposed [22]. The 12-fold rotation symmetry and quasiperiodicity of 30° TBG have been demonstrated by various measurements, such as the Raman spectroscopy, low-energy electron microscopy/diffraction, transmission electron microscopy, and scanning tunneling microscopy measurements [17–19,22,27]. A number of Dirac cones, especially the mirror-symmetric ones, have been observed by the angle-resolved photoemission spectroscopy (ARPES) measurements [17,18]. The quasicrystalline order in 30° TBG can induce unique localization of electrons without any extrinsic

disorders [23,26]. The perfect superlubricity characterized by a scale invariant sliding force is demonstrated theoretically [24]. The quantum oscillations with spiral Fermi surfaces were predicted theoretically due to the quasiperiodicity and weak coupling between layers [29]. The unbalanced electron distributions with characteristic signatures due to Umklapp scatterings are revealed experimentally [25]. All these peculiar properties, especially the quasiperiodicity, make 30° TBG much different from graphene monolayer, although it has electronic properties very similar to those of two decoupled graphene monolayers in the vicinity of the Fermi level [21].

Recently, twisted double bilayer graphene (TDBG) consisting of two AB-stacked bilayers has received much attention especially on the properties [30–34] associated with the strongly correlated electrons in the electrically tunable flat band [35–38], such as the superconductivity, magnetic phase transition, and correlated insulating state. Besides, the TDBG under the electric field was found to be a valley Hall insulator [38]. Generic twisted multilayer graphene, M layers on top of N layers with a twist angle, possesses two topologically nontrivial flat bands, which exhibit a Chern-number hierarchy [39]. Similar to the 30° TBG, the 30° TDBG is expected to possess some striking properties due to the disappearance of the translational symmetry. More importantly, the successful fabrication of 30° TBG and accurate determination of some key structural parameters (such as twist angle, stacking order, and interlayer spacing) in experiments [40,41] ensure the realization of 30° TDBG in the near future.

In this paper, we study the effect of the 30° twisted interface between two AB-stacked graphene bilayers by means of the tight-binding approximation. By comparing with AB-stacked bilayer graphene, we find out that the two subsystems on both sides of the 30° twisted interface almost decouple in the low-energy region. Importantly, there is a strong coupling between them at the Q point and it results in the appearance of some 12-fold-symmetry-like quasicrystalline

*s.yuan@whu.edu.cn

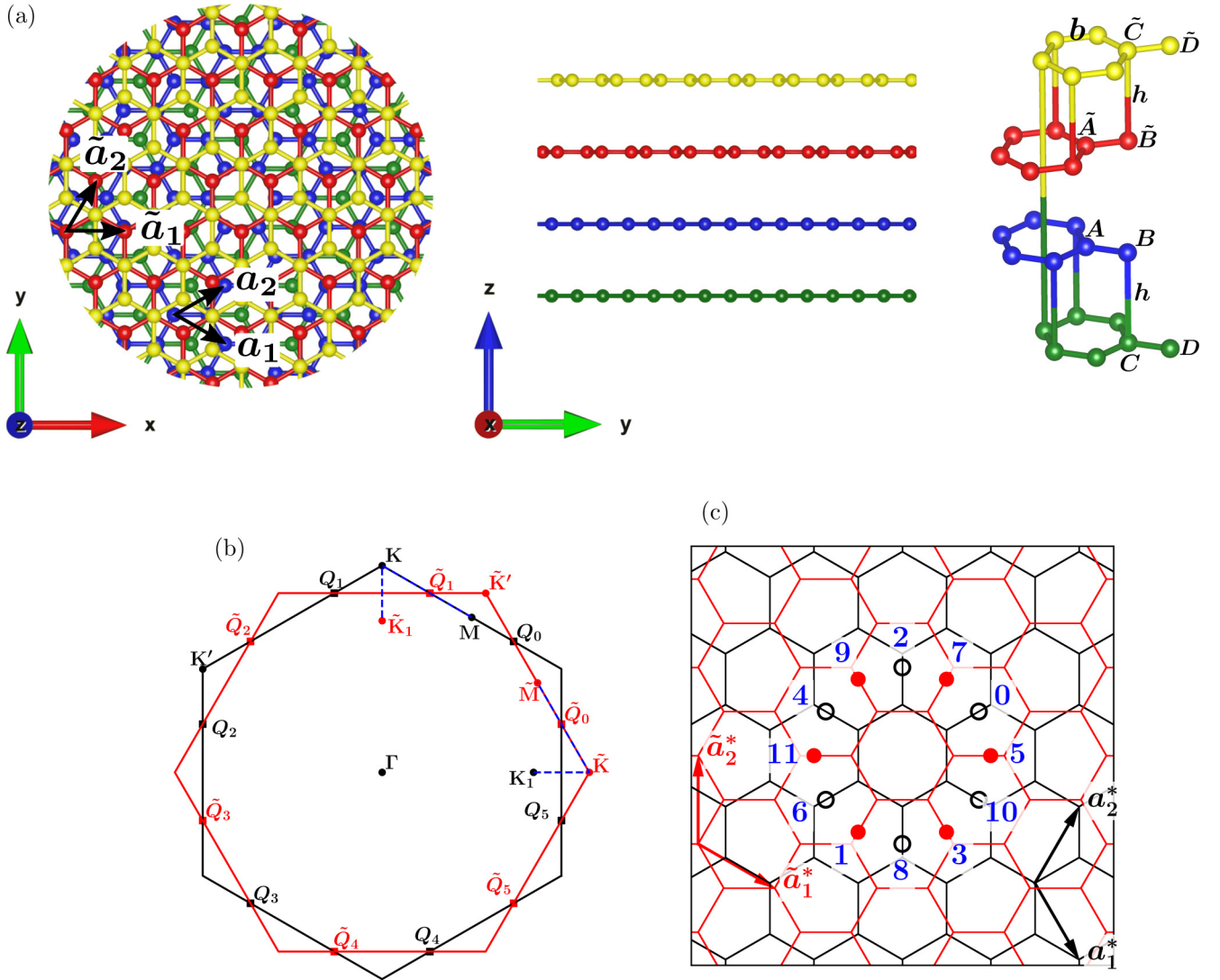


FIG. 1. (a) The top and side views of 30° twisted double bilayer graphene as well as the detailed structure around the rotation center. $b(= a/\sqrt{3})$ is the carbon-carbon bond length and h is the interlayer distance. (b) The Brillouin zones of the bottom and top bilayers with some special points labeled. (c) The locations of the k points of the 12 waves for $\mathbf{k}_0 = 0$. The six k -points of the bottom (top) bilayer are labeled by empty black (solid red) dots. The 12 k -points are folded to the 12 Q points as $\mathbf{k}^{(0)} \rightarrow Q_1, \mathbf{k}^{(1)} \rightarrow \tilde{Q}_5, \mathbf{k}^{(2)} \rightarrow Q_2, \mathbf{k}^{(3)} \rightarrow \tilde{Q}_3, \mathbf{k}^{(4)} \rightarrow Q_3, \mathbf{k}^{(5)} \rightarrow \tilde{Q}_1, \mathbf{k}^{(6)} \rightarrow Q_4, \mathbf{k}^{(7)} \rightarrow \tilde{Q}_2, \mathbf{k}^{(8)} \rightarrow Q_5, \mathbf{k}^{(9)} \rightarrow \tilde{Q}_0, \mathbf{k}^{(10)} \rightarrow Q_0$, and $\mathbf{k}^{(11)} \rightarrow \tilde{Q}_4$.

electronic states. The similar electronic properties also exist in the system of graphene monolayer on AB-stacked bilayer with 30° twist angle (30° AB/G). Two realistic systems, 30° TDBG and 30° AB/G, are introduced to realize the quasicrystalline character.

The rest of the paper is organized as follows. In Sec. II, we describe the structure of 30° TDBG, basic theory, and computational details. In Sec. III, the interlayer decoupling and coupling at both low- and high-energy regions and related discussions are presented. In Sec. IV, we summarize our findings and conclude the paper.

II. MODEL AND METHODS

A. Structure of 30° TDBG

The structure of 30° TDBG is shown in Fig. 1(a). It consists of two AB-stacked graphene bilayers with the top bilayer

twisted by 30° . The stacking of the middle two layers is the same as a 30° TBG. In total, there are two AB-stacked interfaces and one 30° twisted interface in a 30° TDBG. The lattice vectors and reciprocal lattice vectors of the bottom bilayer are

$$\mathbf{a}_1 = a \left(\frac{\sqrt{3}}{2}, -\frac{1}{2} \right), \quad \mathbf{a}_2 = a \left(\frac{\sqrt{3}}{2}, \frac{1}{2} \right), \quad (1)$$

and

$$\mathbf{a}_1^* = \frac{2\pi}{a} \left(\frac{1}{\sqrt{3}}, -1 \right), \quad \mathbf{a}_2^* = \frac{2\pi}{a} \left(\frac{1}{\sqrt{3}}, 1 \right), \quad (2)$$

respectively. $a = 2.456 \text{ \AA}$ is the lattice constant of graphene. The lattice vectors and the reciprocal lattice vectors of the top bilayer are

$$\tilde{\mathbf{a}}_1 = a(1, 0), \quad \tilde{\mathbf{a}}_2 = a \left(\frac{1}{2}, \frac{\sqrt{3}}{2} \right), \quad (3)$$

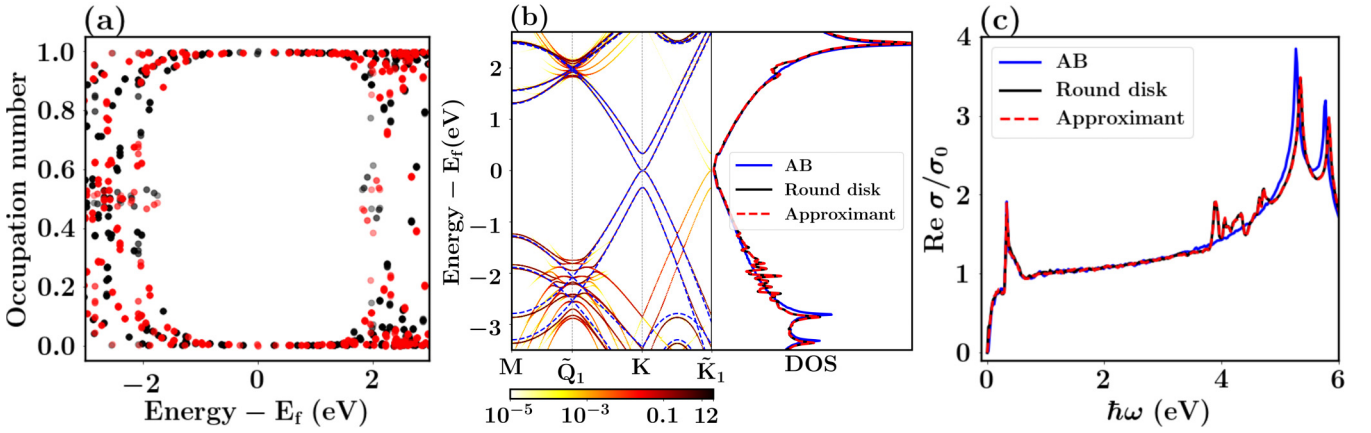


FIG. 2. (a) The occupation numbers of the eigenstates obtained by diagonalizing the Hamiltonian of the 15/26 approximant at Γ point. The black and red dots denote the occupation numbers on the bottom and top bilayers, respectively. (b), (c) The comparisons of the (effective) band structures [left panel in (b)], the density of states [right panel in (b)], and the real part of the optical conductivity σ (c) between 30° twisted double bilayer graphene and AB-stacked bilayer graphene. The results labeled by round disk and approximant are from the round disk with 10 million sites and the 15/26 approximant, respectively. σ is in units of $\sigma_0 = \pi e^2/2h$. The effective band structure is plotted in color in a logarithmic scale.

and

$$\tilde{\mathbf{a}}_1^* = \frac{2\pi}{a} \left(1, -\frac{1}{\sqrt{3}} \right), \quad \tilde{\mathbf{a}}_2^* = \frac{2\pi}{a} \left(0, \frac{2}{\sqrt{3}} \right), \quad (4)$$

respectively. The atomic positions are

$$\begin{aligned} \mathbf{R}_X &= n_1 \mathbf{a}_1 + n_2 \mathbf{a}_2 + \boldsymbol{\tau}_X \quad (\text{bottom bilayer}), \\ \mathbf{R}_{\tilde{X}} &= \tilde{n}_1 \tilde{\mathbf{a}}_1 + \tilde{n}_2 \tilde{\mathbf{a}}_2 + \boldsymbol{\tau}_{\tilde{X}} \quad (\text{top bilayer}), \end{aligned} \quad (5)$$

where n_i and \tilde{n}_i are integers, $X = A, B, C, D$ and $\tilde{X} = \tilde{A}, \tilde{B}, \tilde{C}, \tilde{D}$ stand for the sublattices, and $\boldsymbol{\tau}_X$ and $\boldsymbol{\tau}_{\tilde{X}}$ are the sublattice positions in the unit cell. In this paper, $\boldsymbol{\tau}_X$'s and $\boldsymbol{\tau}_{\tilde{X}}$'s are chosen as

$$\begin{aligned} \boldsymbol{\tau}_A &= \frac{1}{3} \mathbf{a}_1 + \frac{1}{3} \mathbf{a}_2 + h \hat{\mathbf{e}}_z = (b, 0, h), \\ \boldsymbol{\tau}_B &= \frac{2}{3} \mathbf{a}_1 + \frac{2}{3} \mathbf{a}_2 + h \hat{\mathbf{e}}_z = (2b, 0, h), \\ \boldsymbol{\tau}_C &= \frac{2}{3} \mathbf{a}_1 + \frac{2}{3} \mathbf{a}_2 + 0 \hat{\mathbf{e}}_z = (2b, 0, 0), \\ \boldsymbol{\tau}_D &= \mathbf{a}_1 + \mathbf{a}_2 + 0 \hat{\mathbf{e}}_z = (3b, 0, 0), \end{aligned} \quad (6)$$

and

$$\begin{aligned} \boldsymbol{\tau}_{\tilde{A}} &= \frac{1}{3} \tilde{\mathbf{a}}_1 + \frac{1}{3} \tilde{\mathbf{a}}_2 + 2h \hat{\mathbf{e}}_z = \left(\frac{1}{2}a, \frac{1}{2}b, 2h \right), \\ \boldsymbol{\tau}_{\tilde{B}} &= \frac{2}{3} \tilde{\mathbf{a}}_1 + \frac{2}{3} \tilde{\mathbf{a}}_2 + 2h \hat{\mathbf{e}}_z = (a, b, 2h), \\ \boldsymbol{\tau}_{\tilde{C}} &= \frac{2}{3} \tilde{\mathbf{a}}_1 + \frac{2}{3} \tilde{\mathbf{a}}_2 + 3h \hat{\mathbf{e}}_z = (a, b, 3h), \\ \boldsymbol{\tau}_{\tilde{D}} &= \tilde{\mathbf{a}}_1 + \tilde{\mathbf{a}}_2 + 3h \hat{\mathbf{e}}_z = \left(\frac{3}{2}a, \frac{3}{2}b, 3h \right), \end{aligned} \quad (7)$$

where $b = 1.418 \text{ \AA}$ is the nearest-neighbor distance within graphene layer, $h = 3.349 \text{ \AA}$ is the interlayer distance, and $\hat{\mathbf{e}}_z$ is the unit vector along the z axis.

B. 15/26 approximant

In this paper, the 30° TDBG is approximated by a moiré pattern obtained by introducing slight stress to the top bilayer, which changes the lattice constant of the top bilayer from $a = 2.456$ to $\tilde{a} = 2.454 \text{ \AA}$. The moiré pattern is named

a 15/26 approximant [28] due to the commensurate period $15 \times \sqrt{3}a = 26 \times \tilde{a}$ along the x axis, where $\sqrt{3}a$ and \tilde{a} are the basic periods of the bottom and top bilayers, respectively. Accordingly, the elementary unit cell of the 15/26 approximant contains 5404 sites, including 1350×2 sites from the bottom bilayer and 1352×2 sites from the top bilayer.

Because the density of states count the number of the states at certain energy and the optical conductivity contains the information of the amplitude and phase of the wave functions, the validation of an approximant can be verified if these two physical quantities of quasicrystalline can be reproduced accurately. Thus we calculate the density of states and optical conductivity of the 15/26 approximant and compare them with those of a real 30° TDBG [see Fig. 2(b)]. In these calculations, the real 30° TDBG is modeled by a round disk containing about 10 million sites. We remove all the dangling bonds, and in such a huge round disk, the edge effects can be ignored safely.

Besides the 15/26 approximant, the commensurate moiré patterns with the twist angle close to 30° can also be considered as an approximant of 30° TDBG, such as 29.957° and 30.011° TDBGs. A commensurate moiré pattern can be determined by two integers m and n , which are related to the twist angle θ as [1]

$$\cos \theta = \frac{m^2 + 4mn + n^2}{2(m^2 + mn + n^2)}. \quad (8)$$

The twist angles of 29.957° and 30.011° correspond to $(m, n) = (11, 30)$ and $(15, 41)$, respectively. Our calculations shown in the Supplemental Material [42] indicate that both structures can also reproduce the density of states and optical conductivity of 30° TDBG accurately. However, the 15/26 approximant is chosen to study the electronic structure of 30° TDBG, because 29.957° and 30.011° TDBG contain 10 808 and 20 168 sites, which are much more than the site number of 5404 in 15/26 approximant.

C. Tight-binding model

The Hamiltonians of the 30° TDBG and its 15/26 approximant are described by a tight-binding model based on p_z orbitals. The hopping energy between site i and j is determined by [43]

$$t(\mathbf{r}_{ij}) = n^2 V_{pp\sigma}(|\mathbf{r}_{ij}|) + (1 - n^2) V_{pp\pi}(|\mathbf{r}_{ij}|), \quad (9)$$

where n is the direction cosine of relative position vector \mathbf{r}_{ij} with respect to the z axis. The Slater-Koster parameters $V_{pp\sigma}$ and $V_{pp\pi}$ read

$$\begin{aligned} V_{pp\pi}(|\mathbf{r}_{ij}|) &= -\gamma_0 e^{2.218(b-|\mathbf{r}_{ij}|)} F_c(|\mathbf{r}_{ij}|), \\ V_{pp\sigma}(|\mathbf{r}_{ij}|) &= \gamma_1 e^{2.218(h-|\mathbf{r}_{ij}|)} F_c(|\mathbf{r}_{ij}|). \end{aligned} \quad (10)$$

γ_0 and γ_1 are 3.12 and 0.48 eV, respectively. F_c is a smooth function:

$$F_c(r) = (1 + e^{(r-0.265)/5})^{-1}. \quad (11)$$

In our calculations, all the hoppings with the neighbor distance less than 5 Å are under consideration. For 30° TBG, the Fermi velocity and effective band structure calculated using this tight-binding model fit well the experimental results [28]. This tight-binding model has also been justified by comparing results with several experiments [44–46].

D. Tight-binding propagation method

The density of states and optical conductivity are calculated by the tight-binding propagation method (TBPM) [47]. This method is based on the numerical solution of the time-dependent Schrödinger equation without any diagonalization. Both memory and CPU costs scale linearly with the system size, and TBPM is extremely powerful for the calculations of large samples such as quasicrystalline with more than 10 million sites.

In TBPM [47], a random superposition of the p_z orbitals at all sites is used as the initial state $|\phi_0\rangle$ with $\langle\phi_0|\phi_0\rangle = 1$. DOS is calculated as Fourier transform of the time-dependent correlation function

$$d(\epsilon) = \frac{1}{2\pi} \int_{-\infty}^{\infty} e^{i\epsilon\tau} \langle\phi_0|e^{-iH\tau/\hbar}|\phi_0\rangle d\tau. \quad (12)$$

The optical conductivity is calculated by using the Kubo formula in TBPM [47]. The real part of the optical conductivity matrix $\sigma_{\alpha,\beta}$ at temperature T reads

$$\begin{aligned} \text{Re}\sigma_{\alpha,\beta}(\omega) &= \lim_{\epsilon \rightarrow 0^+} \frac{e^{-\hbar\omega/k_B T} - 1}{\hbar\omega A} \int_0^{\infty} e^{-\epsilon\tau} \sin \omega\tau \\ &\quad \times 2\text{Im} \langle j_\alpha \phi_2(\tau) | j_\beta \phi_1(\tau) \rangle d\tau. \end{aligned} \quad (13)$$

Here, A is the area of the unit cell per layer, and $|\phi_1(\tau)\rangle$ and $|\phi_2(\tau)\rangle$ read

$$\begin{aligned} |\phi_1(\tau)\rangle &= e^{-iH\tau/\hbar} [1 - f(H)] |\phi_0\rangle, \\ |\phi_2(\tau)\rangle &= e^{-iH\tau/\hbar} f(H) |\phi_0\rangle, \end{aligned} \quad (14)$$

where $f(H) = 1/(e^{(H-\mu)/k_B T} + 1)$ is the Fermi-Dirac distribution operator and μ is the electronic chemical potential. In this paper, all the optical conductivities are calculated at $T = 300$ K and $\mu = 0$ eV (the charge neutrality point).

E. Band-unfolding process

Although the band structure can be derived directly from the periodic 15/26 approximant, its supercell character relative to the primitive unit cell of graphene results in the fold of the bands. So the band structures calculated directly from the 15/26 approximant cannot be used to compare with the ARPES measurements. To overcome this problem, the band structure of 15/26 approximant is unfolded to the primitive unit cell of graphene as the following procedure.

First, the spectral function at wave vector \mathbf{k} and energy ϵ can be calculated by [48]

$$A(\mathbf{k}, \epsilon) = \sum_{I\mathbf{k}_{\text{SC}}} P_{I\mathbf{k}_{\text{SC}}}(\mathbf{k}) \delta(\epsilon - \epsilon_{I\mathbf{k}_{\text{SC}}}), \quad (15)$$

where $\epsilon_{I\mathbf{k}_{\text{SC}}}$ is the energy for I th band at wave vector \mathbf{k}_{SC} for the approximant. Actually, only one \mathbf{k}_{SC} , namely, $\mathbf{k}_{\text{SC}} = \mathbf{k} + \mathbf{G}_{\text{SC}}$ being \mathbf{G}_{SC} the reciprocal lattice vector of the approximant, contributes to the spectral function. The spectral weight is defined as

$$P_{I\mathbf{k}_{\text{SC}}}(\mathbf{k}) = \sum_s \sum_i |\langle \psi_{ik}^{\text{PC}_s} | \Psi_{I\mathbf{k}_{\text{SC}}}^{\text{SC}} \rangle|^2 = \sum_s P_{I\mathbf{k}_{\text{SC}}}^s(\mathbf{k}), \quad (16)$$

where $|\psi_{ik}^{\text{PC}_s}\rangle$ and $|\Psi_{I\mathbf{k}_{\text{SC}}}^{\text{SC}}\rangle$ are the eigenstates of layer s and the approximant, respectively. Under the tight-binding method, the contribution from layer s is

$$P_{I\mathbf{k}_{\text{SC}}}^s(\mathbf{k}) = \frac{1}{n_s} \sum_{\alpha} \sum_{I_s' \alpha'} e^{i\mathbf{k} \cdot (\mathbf{l}_s - \mathbf{l}_s')} U_{I\mathbf{k}_{\text{SC}}}^{I_s \alpha} U_{I\mathbf{k}_{\text{SC}}}^{I_s' \alpha'}. \quad (17)$$

Here, n_s is the number of the primitive unit cell of layer s inside the elementary unit cell of the approximant. $U_{I\mathbf{k}_{\text{SC}}}^{I_s \alpha}$ is the projection of $|\Psi_{I\mathbf{k}_{\text{SC}}}^{\text{SC}}\rangle$ (the eigenstate of the approximant) on $|\mathbf{k}_{\text{SC}} I_s \alpha\rangle$ (the Bloch basis function of approximant). Equation (17) indicates that only the eigenstates of the approximant are necessary to obtain the spectral function.

Then the effective band structure can be obtained by [49]

$$\delta N(\mathbf{k}, \epsilon) = \int_{\epsilon - \delta\epsilon/2}^{\epsilon + \delta\epsilon/2} A(\mathbf{k}, \epsilon') d\epsilon', \quad (18)$$

where $\delta\epsilon$ is the bin width in energy sampling.

III. RESULTS AND DISCUSSION

A. Interlayer decoupling in the low-energy region

First, the distributions of the eigenstates in the low-energy region are calculated by diagonalizing the Hamiltonian of the 15/26 approximant at the Γ point and the results are shown in Fig. 2(a). All these states around the Fermi level occur inside only the bottom bilayer or the top bilayer, which implies the interlayer decoupling across the 30° twisted interface in the vicinity of the Fermi level. It can be proven further by comparing the (effective) band structures and density of states of the 30° TDBG and AB-stacked bilayer graphene [see Fig. 2(b)]. Both of them show a parabolic touch point at K point. The agreement in the low-energy region means that 30° TDBG should have similar electronic properties to an AB-stacked bilayer graphene, such as the optical conductivity shown in Fig. 2(c).

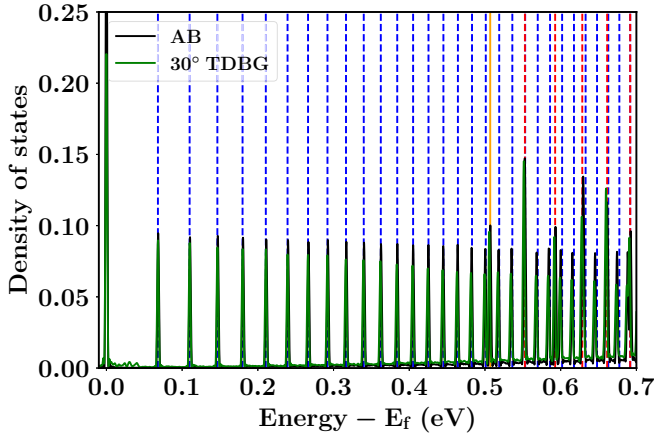


FIG. 3. The density of states of AB-stacked bilayer graphene and 30° TDBG under the magnetic field of 20 T, averaged from ten different initial random states in Eq. (12). The vertical lines show the analytical Landau levels of AB-stacked bilayer. The blue and red dashed lines represent the Landau levels $\epsilon_{n,L,+}$ and $\epsilon_{n,H,+}$ with $n \geq 1$, respectively. The orange solid line is the Landau level $\epsilon_{0,H,+}$. The levels $\epsilon_{0,L}$ and $\epsilon_{-1,L}$ are at zero. Only the electron side is shown due to the electron-hole symmetry in the simplified tight-binding approximation.

The interlayer decoupling across the 30° twisted interface can also be proven by checking the Landau levels (see Fig. 3), which is in good agreement with the numerical and analytical [50] results of an AB-stacked bilayer graphene. To compare with the analytical results, a simplified but often used tight-binding model is adopted. The intralayer hoppings with the nearest-neighbor approximation are adopted. The interlayer hopping across the AB-stacked interfaces with only the vertically arranged neighbors are considered, but for the interlayer hoppings across the 30° twisted interface, all the neighbors with the neighbor distance less than 5 Å are taken into account. The analytical Landau levels shown in Fig. 3 can be classified into three groups [50]. They are (1) $n \geq 1$:

$$\epsilon_{n,\mu,s} = \frac{s}{\sqrt{2}} [\gamma_1^2 + (2n+1)\Delta_B^2 + \mu\sqrt{\gamma_1^2 + 2(2n+1)\gamma_1^2\Delta_B^2 + \Delta_B^4}]^{1/2}, \quad (19)$$

(2) $n = 0$,

$$\epsilon_{0,L} = 0, \quad \epsilon_{0,H,s} = s\sqrt{\gamma_1^2 + \Delta_B^2}, \quad (20)$$

and (3) $n = -1$:

$$\epsilon_{-1,L} = 0. \quad (21)$$

In these equations, $s = \pm 1$ (labeled by \pm) stands for the electron and hole bands, respectively. $\mu = \pm 1$ correspond to the higher and lower subbands in the limit of zero magnetic fields, respectively. We use the notation $\mu = H, L$ instead of \pm to avoid the confusion with $s = \pm$. $\Delta_B = 0.163$ eV (defined by $\sqrt{2\hbar v_f^2 eB}$) is the magnetic energy which corresponds to the Fermi velocity $v_f = 1 \times 10^6$ m/s in graphene. In Fig. 3, only the electron side is shown due to the electron-hole symmetry in this simplified tight-binding model.

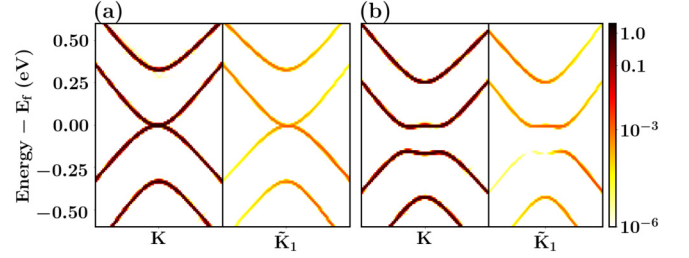


FIG. 4. The comparison of the effective band structures around K and \tilde{K}_1 along the x axis under the electric field of (a) 0 and (b) 0.05 eV/Å. The results are plotted in color in a logarithmic scale.

Although the interlayer decoupling dominates the electronic properties in the low-energy region, the obvious interlayer coupling still exists in the high-energy region, especially around \tilde{Q}_1 point. Actually, 30° TDBG shows the similar electronic structure at all Q points (Q_i and \tilde{Q}_i with $i = 0, \dots, 5$), which deviates from the AB-stacked bilayer graphene obviously. It results in the appearance of the new peaks in both density of states and optical conductivity [see Figs. 2(b) and 2(c)]. The origin of the deviation around Q points will be discussed in the next section.

Similar to 30° TBG [17,18], another important property is the emergence of the energy valley at \tilde{K}_1 , which is mirror symmetric with respect to K point [see Fig. 4(a)] because the energy valley at K' is scattered to \tilde{K}_1 with a strong scattering strength. The interlayer decoupling and energy valley scattering are robust even an electric field is applied perpendicular to the graphene plane [see Fig. 4(b)]. The relative weak signal of the effective band structure around \tilde{K}_1 can still be detected in the experiment, because the mirror-symmetric Dirac cones in 30° TBG with the comparable signal strength have been detected by ARPES measurements in the logarithmic scale [17,18].

B. Interlayer coupling at Q points

The effective band structure of 30° TDBG deviates obviously from the band structure of AB-stacked bilayer graphene around the Q points [see Fig. 2(b)], which implies the strong interlayer coupling across the 30° twisted interface. The k -space tight-binding method [26] is adopted to understand this phenomenon. In this method, a \mathbf{k}_0 -related subspace is spanned by the Bloch basis functions of the bottom and top bilayers $|\mathbf{k}, X\rangle$ and $|\tilde{\mathbf{k}}, \tilde{X}\rangle$ with $\mathbf{k} = \mathbf{k}_0 + \tilde{\mathbf{G}}$ and $\tilde{\mathbf{k}} = \mathbf{k}_0 + \mathbf{G}$, where \mathbf{G} and $\tilde{\mathbf{G}}$ are the reciprocal lattice vectors of the bottom and top bilayers, respectively. So, the interlayer coupling rule [51] $\mathbf{k} + \mathbf{G} = \tilde{\mathbf{k}} + \tilde{\mathbf{G}}$ is always satisfied. The Bloch function is defined by

$$\begin{aligned} |\mathbf{k}, X\rangle &= \frac{1}{\sqrt{N}} \sum_{\mathbf{R}_X} e^{i\mathbf{k}\cdot\mathbf{R}_X} |\mathbf{R}_X\rangle \quad (\text{bottom bilayer}), \\ |\tilde{\mathbf{k}}, \tilde{X}\rangle &= \frac{1}{\sqrt{N}} \sum_{\mathbf{R}_{\tilde{X}}} e^{i\tilde{\mathbf{k}}\cdot\mathbf{R}_{\tilde{X}}} |\mathbf{R}_{\tilde{X}}\rangle \quad (\text{top bilayer}), \end{aligned} \quad (22)$$

where N is the normalization factor and $|\mathbf{R}_X\rangle$ ($|\mathbf{R}_{\tilde{X}}\rangle$) denotes the p_z orbital located at sublattice \mathbf{R}_X ($\mathbf{R}_{\tilde{X}}$).

The Hamiltonian consists of three parts, namely, $H = H_0 + \tilde{H}_0 + U$, where H_0 and \tilde{H}_0 are the Hamiltonians of the bottom and top bilayers, and U is the interaction between the two bilayers. The matrix elements within the bottom bilayer are given,

$$\begin{aligned} \langle \mathbf{k}, X | H_0 | \mathbf{k}', X' \rangle &= h_{XX'}(\mathbf{k}) \delta_{\mathbf{k}, \mathbf{k}'}, \\ h_{XX'}(\mathbf{k}) &= \sum_{\mathbf{L}} t(\mathbf{L} + \boldsymbol{\tau}_{X'X}) e^{i\mathbf{k} \cdot (\mathbf{L} + \boldsymbol{\tau}_{X'X})}, \end{aligned} \quad (23)$$

where $\mathbf{L} = n_1 \mathbf{a}_1 + n_2 \mathbf{a}_2$ and $\boldsymbol{\tau}_{X'X} = \boldsymbol{\tau}_{X'} - \boldsymbol{\tau}_X$, and this form also applies to the top bilayer. The matrix elements between the two bilayers read

$$\langle \mathbf{k}, X | U | \tilde{\mathbf{k}}, \tilde{X} \rangle = \sum_{\tilde{\mathbf{G}}\tilde{\mathbf{G}}} T(\mathbf{k} + \mathbf{G}) e^{i\mathbf{G} \cdot \boldsymbol{\tau}_X - i\tilde{\mathbf{G}} \cdot \boldsymbol{\tau}_{\tilde{X}}} \delta_{\mathbf{k} + \mathbf{G}, \tilde{\mathbf{k}} + \tilde{\mathbf{G}}}, \quad (24)$$

where $T(\mathbf{k} + \mathbf{G})$ is the in-plane Fourier transform of the interlayer hopping function $t(\mathbf{r})$ at vector $\mathbf{k} + \mathbf{G}$. It is defined by

$$T(\mathbf{q}) = \frac{1}{S} \int t(\mathbf{r}_{xy} + Z_{\tilde{X}X} \hat{\mathbf{e}}_z) e^{-i\mathbf{q} \cdot \mathbf{r}_{xy}} d\mathbf{r}_{xy}, \quad (25)$$

where $Z_{\tilde{X}X} = (\boldsymbol{\tau}_{\tilde{X}} - \boldsymbol{\tau}_X) \cdot \mathbf{e}_z$ is the coordinate difference of sublattice \tilde{X} and X along the z axis. For the tight-binding model we adopt, $T(\mathbf{q})$ only depends on the length of \mathbf{q} , namely, $T(\mathbf{q}) = T(|\mathbf{q}|)$.

Under the \mathbf{k}_0 -related subspace spanned by the Bloch basis functions $\{|\mathbf{k}_0 + \tilde{\mathbf{G}}, X\rangle\}$ plus $\{|\mathbf{k}_0 + \mathbf{G}, \tilde{X}\rangle\}$, only the \mathbf{G} 's and $\tilde{\mathbf{G}}$'s with small lengths contribute the Hamiltonian $H(\mathbf{k}_0)$ effectively. In this paper, the 12-wave approximation [26], namely, only considering the \mathbf{G} 's and $\tilde{\mathbf{G}}$'s with the length less than $\frac{4\pi}{\sqrt{3}a}$, is adopted to construct the Hamiltonian, which has been proven to be accurate enough to simulate the 30° TBG [26]. The \mathbf{k} -points of the 12 waves are expressed by

$$\mathbf{k}^{(i)} = \mathbf{k}_0 + \mathbf{G}^{(i)} \quad (i = 0, \dots, 11) \quad (26)$$

and

$$\begin{aligned} \mathbf{G}^{(2j)} &= R\left(\frac{\pi}{3}j\right)\mathbf{G}^{(0)} \quad (j = 0, \dots, 5), \\ \mathbf{G}^{(2j+1)} &= R\left(\frac{\pi}{3}j\right)\mathbf{G}^{(1)} \quad (j = 0, \dots, 5), \\ \mathbf{G}^{(0)} &= \tilde{\mathbf{a}}_1^* + \tilde{\mathbf{a}}_2^*, \quad \mathbf{G}^{(1)} = -\mathbf{a}_2^*, \end{aligned} \quad (27)$$

where $R(\theta)$ is the rotation by an angle θ around the z axis. The strongest interaction $T(\mathbf{q})$ takes place just between $\mathbf{k}^{(i)}$ and $\mathbf{k}^{(i\pm 1)}$. After ignoring the weaker interactions, the Hamiltonian can be expressed by a 48×48 matrix,

$$H(\mathbf{k}_0) = \begin{pmatrix} H^{(0)} & W_{0,1} & & & & & & & & & & W_{11,0}^\dagger \\ W_{0,1}^\dagger & H^{(1)} & W_{1,2} & & & & & & & & & \\ & W_{1,2}^\dagger & H^{(2)} & & & & & & & & & \\ & & & \ddots & \ddots & \ddots & & & & & & \\ & & & & & & W_{9,10}^\dagger & H^{(10)} & & & & W_{10,11} \\ W_{11,0} & & & & & & & W_{10,11}^\dagger & H^{(11)} & & & \end{pmatrix}, \quad (28)$$

where

$$H_{XX'}^{(2j)} = h_{XX'}(\mathbf{k}_0 + \mathbf{G}^{(2j)}) \quad (\text{bottom bilayer}), \quad (29)$$

$$H_{\tilde{X}\tilde{X}'}^{(2j+1)} = h_{\tilde{X}\tilde{X}'}(\mathbf{k}_0 + \mathbf{G}^{(2j+1)}) \quad (\text{top bilayer}),$$

with $j = 0, \dots, 5$ and

$$W_{i,i+1} = T(\mathbf{k}_0 + \mathbf{G}^{(i)} + \mathbf{G}^{(i+1)}) \begin{pmatrix} e^{i\frac{2\pi}{3}} & 1 & 0 & 0 \\ 1 & e^{-i\frac{2\pi}{3}} & 0 & 0 \\ 0 & 0 & 0 & 0 \\ 0 & 0 & 0 & 0 \end{pmatrix}. \quad (30)$$

To relate the previous study on 30° TBG [26], we adopt the sublattice order of (A, B, C, D) or $(\tilde{A}, \tilde{B}, \tilde{C}, \tilde{D})$ for $i \equiv 0$ or $3 \pmod{4}$, and (B, A, C, D) or $(\tilde{B}, \tilde{A}, \tilde{C}, \tilde{D})$ for $i \equiv 1$ or $2 \pmod{4}$. This order makes all the matrices of $W_{i,i+1}$ ($i = 0, \dots, 11$) keep the same form. After the diagonalization of the Hamiltonian, the $E \sim \mathbf{k}_0$ dispersion relationship can be obtained, which is named a quasiband structure to distinguish the effective band structure derived by unfolding the band structure of 15/26 approximant. In Fig. 5, we plot the quasiband structure around $\mathbf{k}_0 = 0$ and compare it with the effective band structure around \tilde{Q}_1 . The good agreement with each other proves the validations of the 12-wave approximation and the 15/26 approximant again.

Let us focus on the case of $\mathbf{k}_0 = 0$. After folding the \mathbf{k} points of the 12 waves to their corresponding first Brillouin zones, the basis set is just the collection of the Bloch functions of the bottom bilayer $\{|\tilde{Q}_i, X\rangle\}$ and the Bloch functions of the top bilayer $\{|\tilde{Q}_i, \tilde{X}\rangle\}$ ($i = 0, \dots, 5$) [see Fig. 1(b)]. The corresponding relationship between the \mathbf{k} points of the 12 waves $\mathbf{k}^{(i)}$ and \tilde{Q}_i (\tilde{Q}_i) is shown in Fig. 1. Due to the energy degeneration of the 12 waves, the strong interaction among them results in the obvious deviation of the effective band structure from AB-stacked bilayer graphene. If the interlayer hoppings across the two AB-stacked interfaces consider only the vertically arranged neighbors, the Hamiltonian $H(\mathbf{k}_0 = 0)$ can be simplified as

$$H^{(i)} = \begin{cases} \begin{pmatrix} 0 & t_0 & 0 & 0 \\ t_0 & 0 & \gamma_1 & 0 \\ 0 & \gamma_1 & 0 & t_0 \\ 0 & 0 & t_0 & 0 \end{pmatrix} & i \equiv 0, 3 \pmod{4} \\ \begin{pmatrix} 0 & t_0 & \gamma_1 & 0 \\ t_0 & 0 & 0 & 0 \\ \gamma_1 & 0 & 0 & t_0 \\ 0 & 0 & t_0 & 0 \end{pmatrix} & i \equiv 1, 2 \pmod{4} \end{cases} \quad (31)$$

and

$$W_{i,i+1} = T_0 \begin{pmatrix} e^{i\frac{2\pi}{3}} & 1 & 0 & 0 \\ 1 & e^{-i\frac{2\pi}{3}} & 0 & 0 \\ 0 & 0 & 0 & 0 \\ 0 & 0 & 0 & 0 \end{pmatrix}, \quad (32)$$

where $t_0 = 0.682\gamma_0$, and $T_0 = 0.157$ eV. Unlike 30° TBG, the Hamiltonian matrix $H^{(i)}$ does not keep the same form at different $\mathbf{k}^{(i)}$ because of the sublattice order we adopt and the symmetry decrease. It makes the Hamiltonian $H(\mathbf{k}_0 = 0)$ lose the symmetry under the rotation of moving $H^{(i)}$ to $H^{(i+1)}$. In the following, we focus on only the valence band due to

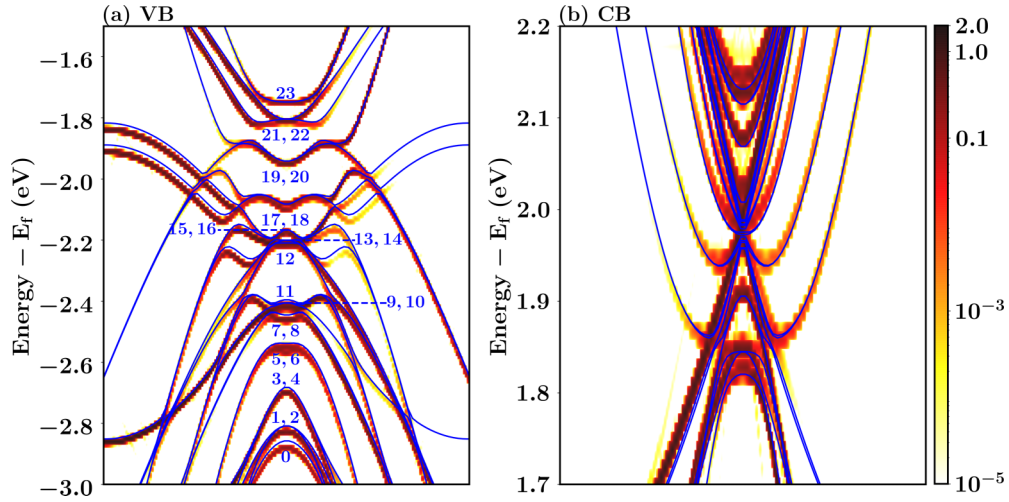


FIG. 5. The comparisons of the effective band structure around \tilde{Q}_1 (plotted in color in a logarithmic scale) and the quasiband structure around $k_0 = 0$ (plotted in blue solid lines) in (a) the valence band and (b) the conduction band. In the valence band, except for the states 0, 11, 12, and 23, any two states marked by $i, i+1$ are degenerate.

the much larger energy splitting in the valence band than that in the conduction band. The 24 electronic states of the valence band are labeled by 0, ..., 23 [see Fig. 5(a)]. Except for states 0, 11, 12, and 23, the others are all twofold degenerate states. The charge distributions of these states are shown in Fig. 6, where (i, j) corresponds to the charge distribution with states i and j occupied at the same time. (i, j) or (m, n) means the two charge distributions have a similar pattern and are plotted in the same subfigure. Comparing with 30° TBG having the point group D_{6d} , all the charge distribution

patterns in 30° TDBG lose the 12-fold symmetry due to the symmetry decrease to point group D_3 . But the corresponding 12-fold-symmetry-like counterparts still exist. For example, the occupation number of the charge distribution 0 on the middle two layers is more than 85%. If the occupations on the bottom and top layers are ignored, this charge distribution pattern still possesses the 12-fold symmetry, which corresponds to the charge distribution $m = 0$ or 6 in 30° TBG [26]. In addition, charge distributions (1,2) and (3,4) have the occupation number on the middle two layers more than 70%,

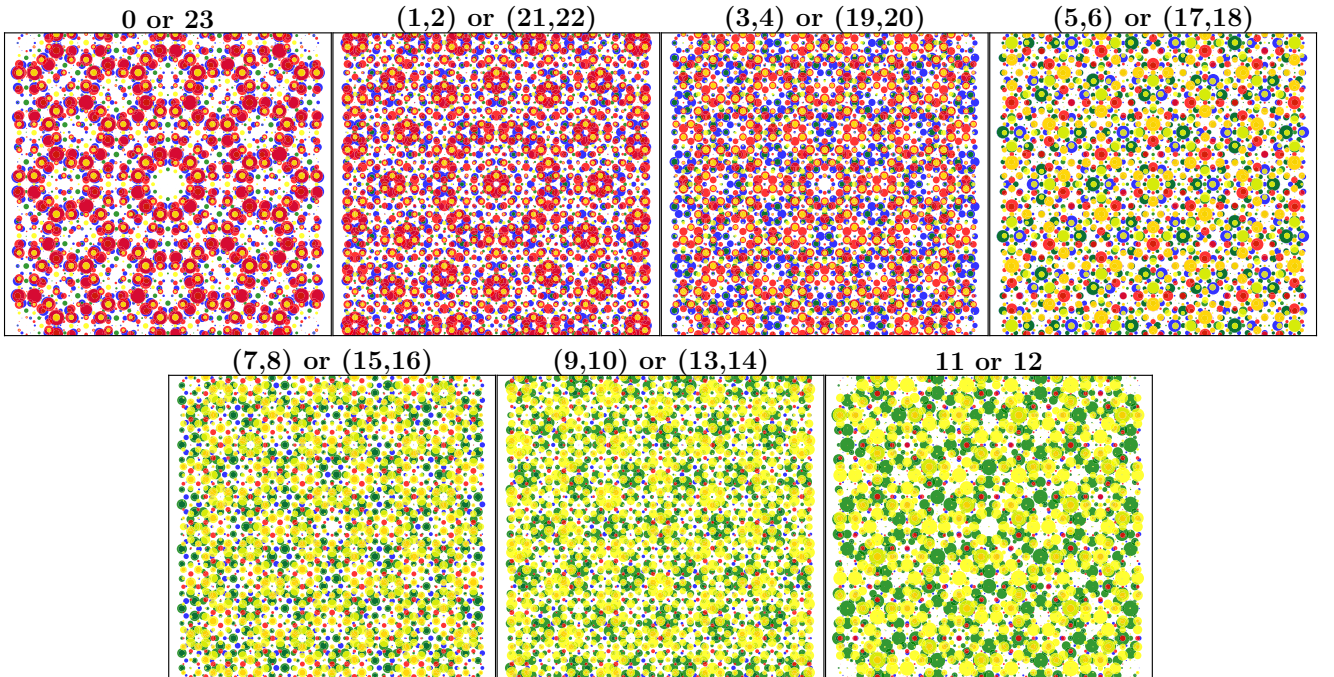


FIG. 6. The charge distributions of the electronic states in the valence band at $k_0 = 0$. The labels of these states are given in Fig. 5(a). The occupations on the four layers from bottom to top are plotted in green, blue, red, and yellow dots. i or j means states i and j have similar charge distribution patterns. (i, j) corresponds to the charge distribution with the states i and j occupied at the same time.

corresponding to cases $m = \pm 1, \pm 5$ and $m = \pm 2, \pm 4$ in 30° TBG [26], respectively. The charge distribution (5,6) is similar to the case $m = \pm 3$ in 30° TBG [26], but shows the similar occupation numbers on the four layers. Importantly, all of the charge distribution patterns (7,8), (9,10), and 11 do not exist in 30° TBG, and there are very little occupation numbers on the middle two layers (less than 20%). These results indicate that the 12-wave interaction results in the strong interlayer coupling across the 30° twisted interface at $k_0 = 0$.

By using the same methods for studying the 30° TDBG, we also calculate the electronic structure of graphene monolayer on AB stacked bilayer graphene with a 30° twist angle (30° AB/G). The results shown in the Supplemental Material [42] indicate that 30° AB/G also shows the interlayer decoupling across the 30° twisted interface in the vicinity of the Fermi level, the strong interlayer coupling at Q points, and the 12-fold-symmetry-like quasicrystalline electronic states. The results imply that it is a general phenomenon in 30° twisted graphene multilayer systems.

IV. CONCLUSION

By means of the tight-binding approximation, we systematically study the electronic properties of 30° TDBG, which are composed of two AB-stacked bilayer graphene with top bilayer twisted by 30° . In the low-energy region, the interlayer decoupling across the 30° twisted interface is proven from various electronic properties, such as the density of states, effective band structure, optical conductivity, and Landau levels. However, the 30° TDBG shows quite a different

effective band structure to an AB-stacked bilayer graphene at Q points due to the 12-wave interaction. It results in the appearance of new van Hove singularities in the density of states and new peaks in the optical conductivity. Importantly, the 12-fold-symmetry-like electronic states, which occur in 30° TBG with exact 12-fold symmetry, can be found in 30° TDBG in spite of the symmetry decrease to the point group D_3 . Moreover, some special electronic states appear in 30° TDBG, which cannot be found in 30° TBG. These states have large occupation numbers on the top and bottom layers but little occupation numbers on the middle two layers. These results demonstrate the strong interlayer coupling across the 30° twisted interface in 30° TDBG at Q points, although it shows interlayer decoupling in the vicinity of the Fermi level.

ACKNOWLEDGMENTS

This work was supported by the National Natural Science Foundation of China (Grant No. 11774269) and the China Postdoctoral Science Foundation (Grant No. 2018M632902). M.I.K. acknowledges support from the JTC-FLAGERA Project GRANSPORT. Numerical calculations presented in this paper have been partially performed on the supercomputing system in the Supercomputing Center of Wuhan University. Support by the Netherlands National Computing Facilities Foundation (NCF) with funding from the Netherlands organisation for Scientific Research (NWO) is gratefully acknowledged.

-
- [1] S. Shallcross, S. Sharma, E. Kandelaki, and O. A. Pankratov, *Phys. Rev. B* **81**, 165105 (2010).
 - [2] C. Berger, Z. Song, X. Li, X. Wu, N. Brown, C. Naud, D. Mayou, T. Li, J. Hass, A. N. Marchenkov, E. H. Conrad, P. N. First, and W. A. de Heer, *Science* **312**, 1191 (2006).
 - [3] J. Hass, F. Varchon, J. E. Millán-Otoya, M. Sprinkle, N. Sharma, W. A. de Heer, C. Berger, P. N. First, L. Magaud, and E. H. Conrad, *Phys. Rev. Lett.* **100**, 125504 (2008).
 - [4] D. L. Miller, K. D. Kubista, G. M. Rutter, M. Ruan, W. A. de Heer, P. N. First, and J. A. Stroscio, *Science* **324**, 924 (2009).
 - [5] M. L. Sadowski, G. Martinez, M. Potemski, C. Berger, and W. A. de Heer, *Phys. Rev. Lett.* **97**, 266405 (2006).
 - [6] M. Sprinkle, D. Siegel, Y. Hu, J. Hicks, A. Tejada, A. Taleb-Ibrahimi, P. Le Fèvre, F. Bertran, S. Vizzini, H. Enriquez, S. Chiang, P. Soukiassian, C. Berger, W. A. de Heer, A. Lanzara, and E. H. Conrad, *Phys. Rev. Lett.* **103**, 226803 (2009).
 - [7] W. A. de Heer, C. Berger, X. Wu, M. Sprinkle, Y. Hu, M. Ruan, J. A. Stroscio, P. N. First, R. Haddon, B. Piot, C. Faugeras, M. Potemski, and J.-S. Moon, *J. Phys. D: Appl. Phys.* **43**, 374007 (2010).
 - [8] M. Sprinkle, J. Hicks, A. Tejada, A. Taleb-Ibrahimi, P. L. Fèvre, F. Bertran, H. Tinkey, M. C. Clark, P. Soukiassian, D. Martinotti, J. Hass, and E. H. Conrad, *J. Phys. D: Appl. Phys.* **43**, 374006 (2010).
 - [9] M. M. van Wijk, A. Schuring, M. I. Katsnelson, and A. Fasolino, *2D Mater.* **2**, 034010 (2015).
 - [10] E. Suárez Morell, J. D. Correa, P. Vargas, M. Pacheco, and Z. Barticevic, *Phys. Rev. B* **82**, 121407(R) (2010).
 - [11] L.-J. Yin, J.-B. Qiao, W.-X. Wang, W.-J. Zuo, W. Yan, R. Xu, R.-F. Dou, J.-C. Nie, and L. He, *Phys. Rev. B* **92**, 201408(R) (2015).
 - [12] R. Bistritzer and A. H. MacDonald, *Proc. Natl. Acad. Sci.* **108**, 12233 (2011).
 - [13] Y. Cao, V. Fatemi, S. Fang, K. Watanabe, T. Taniguchi, E. Kaxiras, and P. Jarillo-Herrero, *Nature* **556**, 43 (2018).
 - [14] H. C. Po, L. Zou, A. Vishwanath, and T. Senthil, *Phys. Rev. X* **8**, 031089 (2018).
 - [15] M. Yankowitz, S. Chen, H. Polshyn, Y. Zhang, K. Watanabe, T. Taniguchi, D. Graf, A. F. Young, and C. R. Dean, *Science* **363**, 1059 (2019).
 - [16] Y. Cao, V. Fatemi, A. Demir, S. Fang, S. L. Tomarken, J. Y. Luo, J. D. Sanchez-Yamagishi, K. Watanabe, T. Taniguchi, E. Kaxiras, R. C. Ashoori, and P. Jarillo-Herrero, *Nature* **556**, 80 (2018).
 - [17] S. J. Ahn, P. Moon, T.-H. Kim, H.-W. Kim, H.-C. Shin, E. H. Kim, H. W. Cha, S.-J. Kahng, P. Kim, M. Koshino, Y.-W. Son, C.-W. Yang, and J. R. Ahn, *Science* **361**, 782 (2018).
 - [18] W. Yao, E. Wang, C. Bao, Y. Zhang, K. Zhang, K. Bao, C. K. Chan, C. Chen, J. Avila, M. C. Asensio, J. Zhu, and S. Zhou, *Proc. Natl. Acad. Sci. USA* **115**, 6928 (2018).
 - [19] Y. Takesaki, K. Kawahara, H. Hibino, S. Okada, M. Tsuji, and H. Ago, *Chem. Mater.* **28**, 4583 (2016).

- [20] S. Pezzini, V. Mišeikis, G. Piccinini, S. Forti, S. Pace, R. Engelke, F. Rossella, K. Watanabe, T. Taniguchi, P. Kim, and C. Coletti, *Nano Lett.* **20**, 3313 (2020).
- [21] B. Deng, B. Wang, N. Li, R. Li, Y. Wang, J. Tang, Q. Fu, Z. Tian, P. Gao, J. Xue, and H. Peng, *ACS Nano* **14**, 1656 (2020).
- [22] F.C. Bocquet, Y.-R. Lin, M. Franke, N. Samiseresht, S. Parhizkar, S. Soubatch, T.-L. Lee, C. Kumpf, and F.S. Tautz, *Phys. Rev. Lett.* **125**, 106102 (2020).
- [23] M. J. Park, H. S. Kim, and S. B. Lee, *Phys. Rev. B* **99**, 245401 (2019).
- [24] E. Koren and U. Duerig, *Phys. Rev. B* **93**, 201404(R) (2016).
- [25] T. Suzuki, T. Iimori, S. J. Ahn, Y. Zhao, M. Watanabe, J. Xu, M. Fujisawa, T. Kanai, N. Ishii, J. Itatani, K. Suwa, H. Fukidome, S. Tanaka, J. R. Ahn, K. Okazaki, S. Shin, F. Komori, and I. Matsuda, *ACS Nano* **13**, 11981 (2019).
- [26] P. Moon, M. Koshino, and Y.-W. Son, *Phys. Rev. B* **99**, 165430 (2019).
- [27] C. Yan, D.-L. Ma, J.-B. Qiao, H.-Y. Zhong, L. Yang, S.-Y. Li, Z.-Q. Fu, Y. Zhang, and L. He, *2D Mater.* **6**, 045041 (2019).
- [28] G. Yu, Z. Wu, Z. Zhan, M. I. Katsnelson, and S. Yuan, *npj Comput. Mater.* **5**, 122 (2019).
- [29] S. Spurrier and N. R. Cooper, *Phys. Rev. B* **100**, 081405(R) (2019).
- [30] X. Liu, Z. Hao, E. Khalaf, J. Y. Lee, Y. Ronen, H. Yoo, D. Haei Najafabadi, K. Watanabe, T. Taniguchi, A. Vishwanath, and P. Kim, *Nature* **583**, 221 (2020).
- [31] Y. Cao, D. Rodan-Legrain, O. Rubies-Bigorda, J. M. Park, K. Watanabe, T. Taniguchi, and P. Jarillo-Herrero, *Nature* **583**, 215 (2020).
- [32] M. S. Scheurer and R. Samajdar, *Phys. Rev. Res.* **2**, 033062 (2020).
- [33] C. Shen, Y. Chu, Q. Wu, N. Li, S. Wang, Y. Zhao, J. Tang, J. Liu, J. Tian, K. Watanabe, T. Taniguchi, R. Yang, Z. Y. Meng, D. Shi, O. V. Yazyev, and G. Zhang, *Nat. Phys.* **16**, 520 (2020).
- [34] G. W. Burg, J. Zhu, T. Taniguchi, K. Watanabe, A. H. MacDonald, and E. Tutuc, *Phys. Rev. Lett.* **123**, 197702 (2019).
- [35] F. Haddadi, Q. Wu, A. J. Kruchkov, and O. V. Yazyev, *Nano Lett.* **20**, 2410 (2020).
- [36] N. R. Chebrolu, B. L. Chittari, and J. Jung, *Phys. Rev. B* **99**, 235417 (2019).
- [37] Y. W. Choi and H. J. Choi, *Phys. Rev. B* **100**, 201402(R) (2019).
- [38] M. Koshino, *Phys. Rev. B* **99**, 235406 (2019).
- [39] J. Liu, Z. Ma, J. Gao, and X. Dai, *Phys. Rev. X* **9**, 031021 (2019).
- [40] L. Brown, R. Hovden, P. Huang, M. Wojcik, D. A. Muller, and J. Park, *Nano Lett.* **12**, 1609 (2012).
- [41] J.-B. Wu, H. Wang, X.-L. Li, H. Peng, and P.-H. Tan, *Carbon* **110**, 225 (2016).
- [42] See Supplemental Material at <https://link.aps.org/supplemental/10.1103/PhysRevB.102.115123> for SI. 29.957° and 30.011° TDBG as approximants of 30° TDBG. SII. Electronic structure of 30° AB/G.
- [43] J. C. Slater and G. F. Koster, *Phys. Rev.* **94**, 1498 (1954).
- [44] G. Trambly de Laissardière, D. Mayou, and L. Magaud, *Phys. Rev. B* **86**, 125413 (2012).
- [45] L. Huder, A. Artaud, T. Le Quang, G. T. de Laissardière, A. G. M. Jansen, G. Lapertot, C. Chapelier, and V. T. Renard, *Phys. Rev. Lett.* **120**, 156405 (2018).
- [46] H. Shi, Z. Zhan, Z. Qi, K. Huang, E. v. Veen, J. Á. Silva-Guillén, R. Zhang, P. Li, K. Xie, H. Ji, M. I. Katsnelson, S. Yuan, S. Qin, and Z. Zhang, *Nat. Commun.* **11**, 371 (2020).
- [47] S. Yuan, H. De Raedt, and M. I. Katsnelson, *Phys. Rev. B* **82**, 115448 (2010).
- [48] H. Nishi, Y.-i. Matsushita, and A. Oshiyama, *Phys. Rev. B* **95**, 085420 (2017).
- [49] P. V. C. Medeiros, S. Stafström, and J. Björk, *Phys. Rev. B* **89**, 041407(R) (2014).
- [50] M. Koshino and T. Ando, *Phys. Rev. B* **77**, 115313 (2008).
- [51] M. Koshino, *New J. Phys.* **17**, 015014 (2015).